



Blocking CHOP-dependent TXNIP shuttling to mitochondria attenuates albuminuria and mitigates kidney injury in nephrotic syndrome

Sun-Ji Park^a, Yeawon Kim^a, Chuang Li^a, Junwoo Suh^b, Jothilingam Sivapackiam^c, Tassia M. Goncalves^d, George Jarad^a, Guoyan Zhao^{d,e}, Fumihiko Urano^f, Vijay Sharma^{c,g,h,1}, and Ying Maggie Chen^{a,i,1}

Edited by Qais Al-Awqati, Columbia University Irving Medical Center, New York, NY; received September 9, 2021; accepted July 15, 2022 by Editorial Board Member Andrew R. Marks

Albuminuria is a hallmark of glomerular disease of various etiologies. It is not only a symptom of glomerular disease but also a cause leading to glomerulosclerosis, interstitial fibrosis, and eventually, a decline in kidney function. The molecular mechanism underlying albuminuria-induced kidney injury remains poorly defined. In our genetic model of nephrotic syndrome (NS), we have identified CHOP (C/EBP homologous protein)-TXNIP (thioredoxin-interacting protein) as critical molecular linkers between albuminuria-induced ER dysfunction and mitochondria dyshomeostasis. TXNIP is a ubiquitously expressed redox protein that binds to and inhibits antioxidant enzyme, cytosolic thioredoxin 1 (Trx1), and mitochondrial Trx2. However, very little is known about the regulation and function of TXNIP in NS. By utilizing *Chop*^{-/-} and *Txnip*^{-/-} mice as well as ⁶⁸Ga-Galuminos, our molecular imaging probe for detection of mitochondrial reactive oxygen species (ROS) in vivo, we demonstrate that CHOP up-regulation induced by albuminuria drives TXNIP shuttling from nucleus to mitochondria, where it is required for the induction of mitochondrial ROS. The increased ROS accumulation in mitochondria oxidizes Trx2, thus liberating TXNIP to associate with mitochondrial nod-like receptor protein 3 (NLRP3) to activate inflammasome, as well as releasing mitochondrial apoptosis signal-regulating kinase 1 (ASK1) to induce mitochondria-dependent apoptosis. Importantly, inhibition of TXNIP translocation and mitochondrial ROS overproduction by CHOP deletion suppresses NLRP3 inflammasome activation and p-ASK1-dependent mitochondria apoptosis in NS. Thus, targeting TXNIP represents a promising therapeutic strategy for the treatment of NS.

TXNIP | CHOP | mitochondria | ER stress | Trx2

Nephrotic syndrome (NS), characterized by heavy proteinuria/albuminuria due to various underlying pathologies, is one of the leading causes of chronic kidney disease (CKD) that occurs in ~10% of the population and is associated with significant morbidity and mortality (1). Untreated heavy albuminuria is strongly linked to glomerulosclerosis, interstitial fibrosis, and progressive loss of kidney function (2). In the past 2 decades, angiotensin-converting enzyme inhibitors (ACEIs) and angiotensin II receptor blockers (ARBs) have remained the mainstay to control proteinuria. These agents can decrease proteinuria primarily through reducing intraglomerular pressure hemodynamically after blockade of the renin-angiotensin system. As a result, they are incapable of completely eliminating proteinuria, and their antiproteinuric effect is weak. In addition, ACEIs/ARBs can be challenging to use in patients with advanced kidney disease due to further reduction of glomerular filtration rate and increased risk of hyperkalemia. Thus, identification of more novel drug targets for the treatment of NS is warranted.

Although the molecular link between albuminuria and kidney failure remains elusive, emerging evidence has supported a central role of the tubular epithelial cell (TEC) response to excessive filtered albumin in the progression of proteinuric kidney disease, which is consistent with clinical studies that have shown that decline of kidney function correlates more closely with the tubulointerstitial fibrosis than with the glomerular damage (2). Filtered albumin is reabsorbed by TECs, primarily occurring in the proximal tubules via apical endocytic receptor (megalin/cubilin)-mediated, clathrin-dependent endocytosis (3) and fluid-phase (clathrin-negative) neonatal Fc receptor-mediated transcytosis (4). Additionally, albumin uptake takes place in distal/collecting tubular cells (5). Emerging evidence has highlighted that reclaimed albumin inside the proximal tubular cells (PTCs) activates endoplasmic reticulum (ER) stress and unfolded protein response (UPR) (6–9). The UPR is initiated by three ER transmembrane proteins, PKR-like ER kinase (PERK), inositol-requiring enzyme-1 (IRE1), and activating transcription factor 6 (ATF6), and activates

Significance

Albuminuria is the hallmark of nephrotic syndrome (NS), a leading cause of chronic kidney disease affecting 500 million people worldwide. Thus, there is a clear need to discover novel drug targets to treat proteinuric kidney disease. We demonstrate that thioredoxin-interacting protein (TXNIP), a redox protein that forms the complex with antioxidant oxidoreductase thioredoxin (Trx), relocates from nucleus to mitochondria when C/EBP homologous protein (CHOP), a major endoplasmic reticulum (ER) stress-associated transcription factor, is induced by albuminuria. TXNIP shuttling to mitochondria is essential for mitochondrial reactive oxygen species (ROS) production, which oxidizes mitochondrial-specific Trx2 and disrupts the association between Trx2-TXNIP and Trx2-ASK1 in mitochondria, leading to NLRP3 inflammasome activation and mitochondria-dependent apoptosis. Thus, TXNIP is a potential target to treat NS.

This article is a PNAS Direct Submission. Q.A.-A. is a guest editor invited by the Editorial Board.

Copyright © 2022 the Author(s). Published by PNAS. This article is distributed under Creative Commons Attribution-NonCommercial-NoDerivatives License 4.0 (CC BY-NC-ND).

¹To whom correspondence may be addressed. Email: ychen32@wustl.edu or sharnav@wustl.edu.

This article contains supporting information online at <http://www.pnas.org/lookup/suppl/doi:10.1073/pnas.2116505119/-DCSupplemental>.

Published August 22, 2022.

three distinct signaling branches, PERK-eIF2 α -ATF4, IRE1 α -Xbp1s, and p90ATF6-p50ATF6 (10). Cells rendered dysfunctional due to intense or sustained ER stress are eliminated by ER stress-induced apoptosis, including C/EBP homologous protein (CHOP), JNK, and caspase-12 apoptotic pathways (10).

CHOP is a member of the C/EBP family of transcription factors, which are characterized by the presence of the bZIP domain containing a DNA-contacting basic region and a leucine zipper dimerization module (11). CHOP dimerizes and inhibits other C/EBP proteins, including C/EBP α and β , from binding to their target DNA sequences. It has been shown that the consensus sequences for CHOP-C/EBP α binding are RRRTGCAATMCCC (R, purine; M, adenine or cytosine) (12). For some target genes, CHOP possesses a transcriptional activation domain, which is inducible by stress and functions in isolation from its associated C/EBP dimerization partners (12). Thus, CHOP may serve a dual role both as a dominant inhibitor of DNA binding by C/EBP proteins and as a direct activator of some target genes under stress. In this study, we have identified thioredoxin-interacting protein (TXNIP) as a downstream effector that mediates the action of CHOP during NS.

TXNIP is an important regulator of the cellular redox state. It binds to and inhibits thioredoxin (Trx)-1 and Trx-2, the two isoforms of ubiquitous antioxidant thiol oxidoreductase localized to the cytosol and mitochondria, respectively (13), thereby resulting in increased oxidative stress. In diabetes and pancreatic β cells, TXNIP is induced by high glucose and ER stress and functions as a critical signaling node that links ER stress and inflammation (14). However, the molecular mechanism by which TXNIP activates inflammation has not been elucidated in vivo. Genetic TXNIP deletion protects mice from diabetes (15). Related to kidney disease, it has been shown that inhibition of TXNIP attenuates homocysteine-induced TXNIP-Nod-like receptor protein 3 (NLRP3) binding and NLRP3 inflammasome formation in cultured podocytes. Moreover, TXNIP blockade in vivo attenuates glomerular NLRP3 inflammasome activation and glomerular injury when mice are fed with folate-free diet to induce hyperhomocysteinemia (16). Interestingly, when *Txnip*^{-/-} mice are rendered diabetic, TXNIP deficiency protects against progression of diabetic nephropathy (DN) (17). Whether TXNIP plays a critical pathophysiological role in NS has not been studied.

To investigate the function of TXNIP in NS, we utilized a genetic NS model, *Lamb2*^{-/-} mice, which recapitulate human Pierson syndrome (Online Mendelian Inheritance in Man (OMIM) 609049) that is caused by *LAMB2* mutations and characterized by congenital NS/diffuse mesangial sclerosis with ocular and neurological manifestations (18). *LAMB2* encoding laminin β 2 is one of the leading mutated genes in hereditary NS (19). Laminins are heterotrimeric glycoproteins containing one α , one β , and one γ chain. The major laminin heterotrimer in the mature glomerular basement membrane (GBM) is laminin α 5 β 2 γ 1, or LM-521, synthesized and secreted by both podocytes and glomerular endothelial cells. Laminin trimerization occurs in the ER and involves association of the three chains along their laminin coiled-coil domains to form the long arm. In adult kidneys, LM-511 (α 5 β 1 γ 1) is found throughout all tubular and collecting duct basement membranes, and LM-111 (α 1 β 1 γ 1) is also contained in basement membranes of proximal tubule and loops of Henle (20). Thus, in *Lamb2*^{-/-} mice, tubular basement membranes are not affected. In all cases, *Lamb2*^{-/-} mice also carry a muscle-specific wild-type (WT) rat β 2 transgene (MCK-*Lamb2*) that rescues the otherwise lethal neuromuscular junction defects (21). By utilizing this highly reproducible and penetrant monogenic NS mouse model, the aim of this study was to determine the regulation, functional impact, and potential therapeutic implication of TXNIP in NS.

Results

TXNIP Is Induced by Albuminuria in NS Models. Although it has been shown that albuminuria/proteinuria induces ER stress in kidney cells, results as to participation of specific UPR pathways were conflicting in different in vivo and in vitro studies (6–9). To determine the UPR branches regulating albuminuria-induced ER stress response, we isolated glomeruli and renal tubules from *Lamb2*^{-/-} mice at postnatal day 25 (P25), when the mice had developed significant proteinuria. Immunoblot analysis revealed that the active form of ATF6 (p50ATF6) was increased in both glomeruli and tubules of *Lamb2*^{-/-} mice compared to their WT littermates (Fig. 1 *A* and *B*). In contrast, other UPR branches, phospho-IRE1 α (p-IRE1 α)/XBP1s, as well as phospho-eIF2 α (p-eIF2 α)/ATF4, were not activated in response to albuminuria in both glomeruli (*SI Appendix, Fig. S1A*) and tubules (*SI Appendix, Fig. S2A*) in *Lamb2*^{-/-} mice. Given that sustained ER stress can induce activation of CHOP, JNK, or caspase 12 proapoptotic signaling, we further delineated which ER stress-mediated apoptotic pathway was involved in albuminuria-induced kidney injury. We observed that *Lamb2*^{-/-} glomeruli and tubules exhibited a marked up-regulation of CHOP (Fig. 1 *A* and *B*), but not activation of p-JNK and caspase 12 (*SI Appendix, Figs. S1B* and *S2B*), compared with WT glomeruli and tubules, respectively. Consistent with the protein expression levels, we found that CHOP transcript levels in *Lamb2*^{-/-} mice were increased in both glomeruli (Fig. 1 *C*) and tubules (Fig. 1 *D*) versus that in WT controls.

In agreement with previous reports of intracellular albumin uptake by tubular cells (22) and podocytes (23), dual immunofluorescence (IF) staining of albumin with basement membrane marker laminin α 5 (Lam α 5) that stains both glomerular and tubular basement membranes or podocyte nucleus marker WT-1 highlighted albumin reabsorption inside renal tubules (Fig. 1 *E*), and podocytes (Fig. 1 *F*, arrow), in *Lamb2*^{-/-} mice at P25. To mimic the in vivo condition of podocytes and tubular cells exposed to albuminuria, we employed the in vitro model of albumin overload. When mouse primary podocytes or TECs were incubated with bovine serum albumin (BSA) for 24 h, protein levels of p50ATF6 and CHOP were increased by the treatment of BSA in a dose- and time- dependent manner (Fig. 1 *G* and *H*), which recapitulated the in vivo findings. Absence of β 2 chain may cause defective laminin trimerization in the ER of podocytes and impaired secretion. To make sure that the observed ER stress in podocytes was due to albuminuria, rather than arising from ER retention of excess laminin α and γ chains, we checked ER stress response in passage 0 primary podocytes isolated from WT and *Lamb2*^{-/-} mice at P25. We did not detect involvement of ATF6-CHOP signaling in primary mutant podocytes (*SI Appendix, Fig. S3A*). We also confirmed that primary *Lamb2*^{-/-} TECs did not exhibit activation of ATF6-CHOP axis (*SI Appendix, Fig. S3B*). Together, these results demonstrate that ATF6-CHOP signaling is selectively activated in both glomeruli and tubules responding to albuminuria.

Albuminuria is associated with inflammation in patients with kidney disease (24). Given that in diabetes, TXNIP is a molecular linker between ER stress and inflammation, we therefore speculated that TXNIP might be induced by albuminuria and mediates inflammation in proteinuric kidney disease. Indeed, when primary cells were treated with BSA, a significant induction of TXNIP expression was observed in both podocytes (Fig. 1 *I*) and TECs (Fig. 1 *J*). In line with the in vitro findings, TXNIP exhibited increased abundance in glomeruli in a podocyte distribution pattern as demonstrated by colocalization with the podocyte nucleus marker WT-1 (Fig. 1 *K*, blue arrows), as

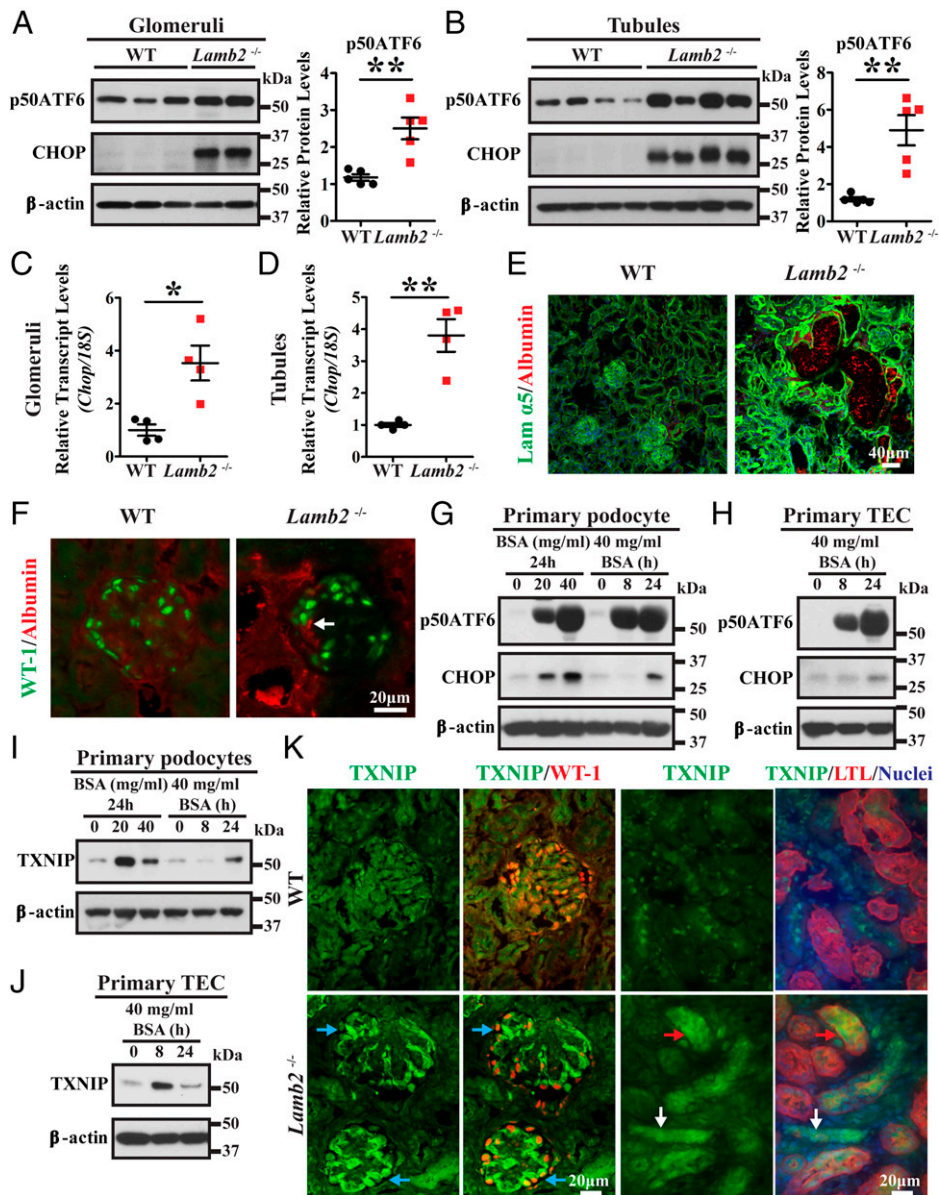


Fig. 1. TXNIP is induced by albuminuria in a model of hereditary NS. (A–D) Glomeruli and tubules were isolated from WT and *Lamb2*^{-/-} mice at P25. (A and B) Representative immunoblots of p50ATF6, CHOP, and β-actin expression in isolated glomeruli (A) and tubules (B) of the indicated genotypes. Densitometry analysis of p50ATF6 in A and B, mean ± SD (*n* = 5 mice per genotype). ***P* < 0.01. (C and D) Quantitative PCR analysis of relative transcript level of *Chop* in isolated glomeruli (C) and tubules (D) of the indicated genotypes. Gene expression was normalized to 18S. Mean ± SD (*n* = 4 mice per genotype). **P* < 0.05; ***P* < 0.01. (E) Dual IF images of albumin (red) and laminin α5 (green) on frozen kidney sections of WT and *Lamb2*^{-/-} mice at P25 by confocal microscopy. (Scale bar, 40 μm.) (F) Dual IF staining of albumin (red) and WT1 (green) on frozen kidney sections. Arrow points to the albumin staining inside podocytes. (Scale bar, 20 μm.) (G–J) Primary mouse podocytes and TECs were isolated and cultured. Cultured primary podocytes (G and I) and TECs (H and J) were starved for 16 h and then treated with 20 or 40 mg/mL BSA for 8 or 24 h. Cell lysates were analyzed by WB for levels of p50ATF6, CHOP, TXNIP, and β-actin. The WB image shown is representative of at least three independent experiments. (K) Representative IF images of frozen kidney sections stained for TXNIP (green) with WT-1 (red), as well as TXNIP (green) with LTL (red) and a nuclear counterstain (blue), from WT and *Lamb2*^{-/-} mice at P25. Blue arrows indicate TXNIP staining in podocytes. Red and white arrows indicate TXNIP staining in LTL-positive and LTL-negative tubules, respectively. (Scale bar, 20 μm.)

well as in both lotus tetragonolobus lectin (LTL)-positive proximal tubules (Fig. 1K, red arrows) and LTL-negative renal tubules (Fig. 1K, white arrows) in *Lamb2*^{-/-} mice at P25, compared with WT littermates.

To explore whether CHOP and TXNIP were also induced in a model of acquired proteinuria, we utilized Adriamycin (ADR)-induced focal segmental glomerulosclerosis (FSGS)/NS model. Male Balb/cJ mice at 10 wk of age were injected intravenously with ADR (12 mg/kg) or saline (vehicle). In the ADR-injected mice, urinary albumin to creatinine ratio was significantly elevated on day 7 postinjection as compared with saline-injected controls, and albuminuria became progressively heavier on day 11 vs. day 7 (SI Appendix, Fig. S4A). On day 11, segmental mesangial matrix expansion and glomerulosclerosis and global glomerulosclerosis, as well as prominent tubular protein casts, appeared in the ADR-treated mice (SI Appendix, Fig. S4B). Meanwhile, Western blots (WBs) of kidney lysates demonstrated increased expression of CHOP and TXNIP in the mice injected with ADR compared with controls (SI Appendix, Fig. S4C). Double IF staining clearly showed induction of TXNIP in podocytes (SI Appendix, Fig. S4D, white arrows) and renal

tubules (SI Appendix, Fig. S4E, white arrows) 11 d after ADR injection. Moreover, kidney mitochondrial fractions showed increased abundance of TXNIP in the mice subjected to ADR compared to controls (SI Appendix, Fig. S4F). Overall, these findings indicate that TXNIP is stimulated in NS mouse models.

TXNIP Gene Expression Correlates with Disease Severity and Decline of Kidney Function in Human Proteinuric Kidney Disease. We next asked whether TXNIP might be relevant in human proteinuric kidney disease by mining gene expression profiles in Nephroseq (<https://www.nephroseq.org>), a publicly available database. TXNIP gene expression was significantly increased in either glomeruli or tubulointerstitium across a spectrum of kidney disease, including CKD, glomerulosclerosis, and DN (Fig. 2A). Interestingly, TXNIP mRNA level in the tubulointerstitium was significantly elevated in patients with nephrotic-range proteinuria versus subnephrotic-range proteinuria in human DN, lupus nephritis (LN), and FSGS samples (Fig. 2A), indicating that TXNIP gene induction may be dependent on the severity of albuminuria/proteinuria, rather than a specific etiology of kidney

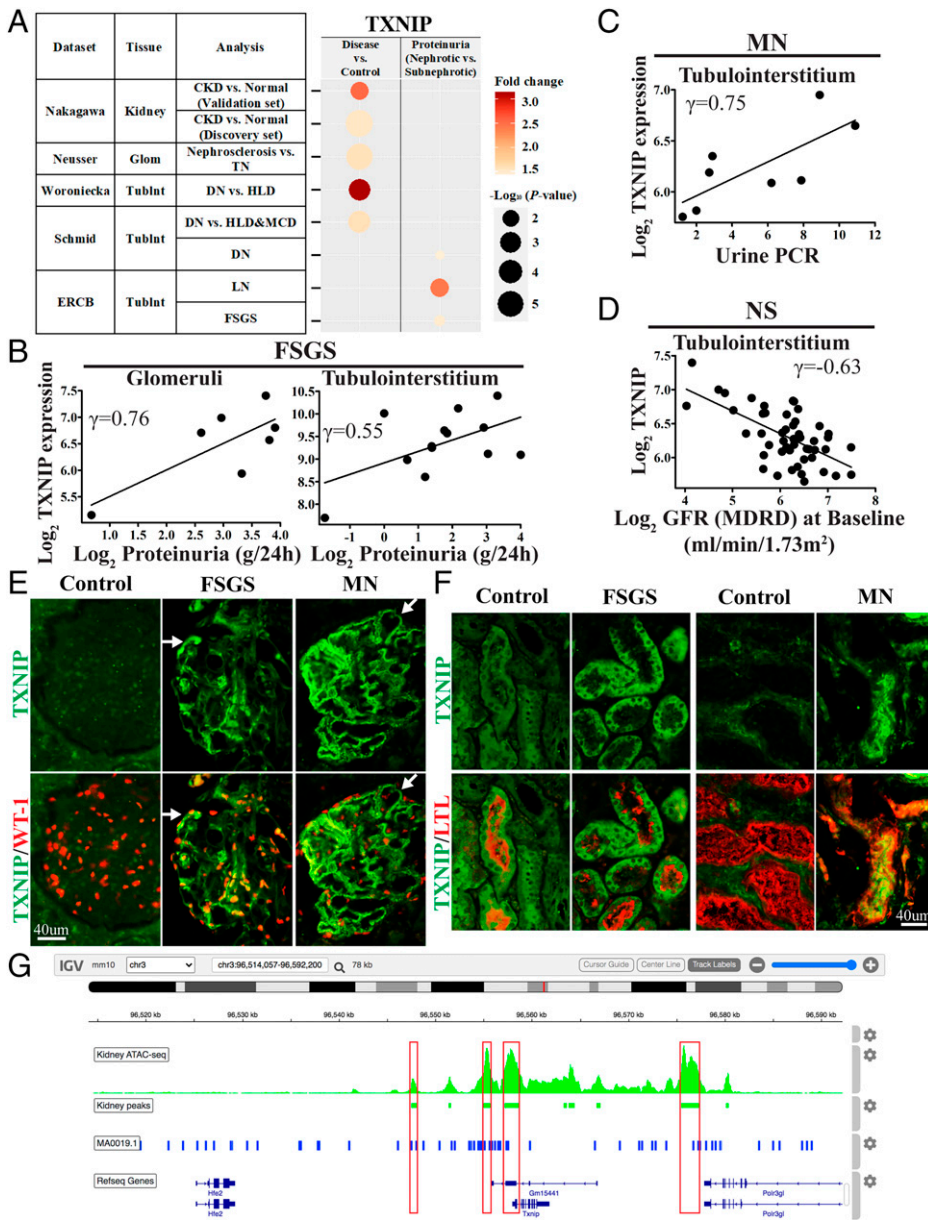


Fig. 2. The relevance of TXNIP up-regulation in human proteinuric kidney disease. (A) Summary of Nephroseq (version 5) data filtered for $P < 0.05$, fold change > 1.5 (disease versus control or nephrotic proteinuria versus subnephrotic proteinuria) in human kidney disease samples. TubInt, tubulointerstitium; Glom, glomeruli; TN, tumor nephrectomy; HLD, healthy living donor; MCD, minimal change disease; FSGS, focal segmental glomerulosclerosis. (B) Scatterplot showing the correlation between glomerular or tubulointerstitial TXNIP gene expression and proteinuria in human FSGS samples. Data were filtered for $P < 0.05$, $\gamma > 0.5$. (C) Scatterplot showing the correlation between TXNIP gene expression in tubulointerstitium and proteinuria in human MN samples. Data were filtered for $P < 0.05$, $\gamma > 0.5$. (D) Scatterplot showing the correlation between TXNIP gene expression in tubulointerstitium and Log₂ GFR (MDRD) in human NS. Data were filtered for $P < 0.05$, $\gamma = -0.63$. (E) Representative images that show the glomerular TXNIP expression (green) costained with WT-1 (red) from healthy nephrectomy versus human FSGS and MN patients, visualized by IF staining on frozen kidney sections. (Scale bar, 40 μ m.) (F) Representative images that show tubular TXNIP expression (green) costained with LTL (red), visualized by IF staining on paraffin kidney sections from healthy nephrectomy versus human FSGS patient, as well as on frozen kidney sections from healthy nephrectomy versus human MN patient. (Scale bar, 40 μ m.) (G) Putative CHOP binding site analysis. Red boxes indicate the overlapping regions between CHOP-C/EBP α binding sites (blue bars) and chromatin accessible sites (green bars) in adult mouse kidney cells.

disease. We further explored the importance of TXNIP gene up-regulation in patients with NS, including FSGS and membranous nephropathy (MN). Notably, in human FSGS samples, a strong positive correlation between glomerular TXNIP transcript level and proteinuria (Pearson correlation coefficient $\gamma = 0.76$, $P = 0.047$) (Fig. 2B) and a moderate positive correlation between tubular TXNIP mRNA level and proteinuria ($\gamma = 0.55$, $P = 0.05$) (Fig. 2B) were observed. In human MN samples, tubular TXNIP gene expression showed a strong positive correlation with urine protein to creatinine ratios (PCR) ($\gamma = 0.75$, $P = 0.03$) (Fig. 2C). More importantly, in NS patients, a strong inverse correlation was found between tubulointerstitial TXNIP gene expression and estimated glomerular filtration rate (eGFR) based on the Modification of Diet in Renal Disease (MDRD) equation ($\gamma = -0.63$, $P < 0.0001$) (Fig. 2D). Co-IF staining of TXNIP with WT-1 or LTL confirmed strikingly increased expression of TXNIP in podocytes (Fig. 2E, white arrows) or renal tubules (Fig. 2F) in human FSGS and MN patients.

We further performed bioinformatics analysis to explore whether TXNIP is potentially regulated by CHOP at the transcriptional level. ATAC-seq (assay for transposase-accessible

chromatin with high-throughput sequencing) peaks represent open chromatin regions that likely contain active regulatory sequences for the corresponding tissues. Single-cell profiling of genome-wide chromatin accessibility of adult mouse kidney tissue demonstrated high chromatin openness of the TXNIP genomic region but not that of the neighboring genes, *Hfe2* and *Polr3gl* (Fig. 2G) (25). Multiple ATAC-seq peaks from kidney tissues were detected in the TXNIP genomic region (Fig. 2G, green bars). Next, we searched the TXNIP genomic region for putative CHOP binding sites using position weight matrices (PWMs) of CHOP obtained from the JASPAR database (<https://jaspar.genereg.net>) (26). PWM MA0019.1 from the JASPAR database represents binding specificity of the heterodimer between CHOP and C/EBP α derived from rat. Since transcription factors from the same family usually have similar binding specificity irrespective of species (27), we used this PWM as input to identify candidate CHOP-C/EBP α binding sites using bioinformatics tool Patser (28). As shown in Fig. 2G, red boxes indicate the overlapping regions between CHOP-C/EBP α heterodimer binding sites (blue bars) and chromatin accessible sites in adult mouse kidney cells (green bars),

suggesting that CHOP-C/EBP α could regulate TXNIP transcription through these bindings sites. These analyses are consistent with the notion that CHOP may serve as an inhibitor of the ability of C/EBP proteins to activate some target genes (12). Taken together, these data support that TXNIP may play an important role in mediating the deleterious effect of albuminuria and that TXNIP gene expression may be directly regulated by the CHOP heterodimer.

CHOP Deletion Attenuates TXNIP Expression and Mitigates Albuminuria, as Well as Improves Kidney Function and Life Span in *Lamb2*^{-/-} Mice. To directly test the role of CHOP on regulation of TXNIP in vivo and their functional impact on albuminuria and kidney function, we bred *Chop*^{-/-} with *Lamb2*^{+/-} mice (*Lamb2*^{-/-} mice died before 6 wk of age) to eventually generate *Lamb2*^{-/-} and *Lamb2*^{-/-};*Chop*^{-/-} mice, as well as their WT littermates. *Lamb2*^{-/-};*Chop*^{-/-} tubules (Fig. 3 *A* and *C*) and glomeruli (Fig. 3 *B* and *D*) showed a dramatic reduction of TXNIP expression at both transcriptional (Fig. 3 *A* and *B*) and translational (Fig. 3 *C* and *D*) levels compared with the *Lamb2*^{-/-} counterparts, which was in alignment with the bioinformatics

analysis of potential regulatory function of CHOP on the TXNIP transcription (Fig. 2*G*). Next, we characterized the phenotype difference between the single and double knockout mice by determining spot urinary albumin to creatinine ratio, serum albumin, and kidney function marker, blood urea nitrogen (BUN) at P25. As shown in Fig. 3 *E–G*, CHOP deletion resulted in decreased albuminuria, increased serum albumin, and improved kidney function in *Lamb2*^{-/-} mice. Moreover, lack of CHOP in *Lamb2*^{-/-} mice significantly prolonged their survival (Fig. 3*H*). Finally, light and transmission electron microscopy (TEM) were used to examine renal histopathology and ultrastructure in the indicated groups at P25. Light microscopic examination of hematoxylin and eosin (H&E)-stained kidney sections revealed severe glomerulosclerosis in *Lamb2*^{-/-} mice. In contrast, *Lamb2*^{-/-};*Chop*^{-/-} mice exhibited less diffuse mesangial matrix expansion (Fig. 3*I*). Periodic acid–Schiff (PAS) staining showed much fewer tubular protein casts in *Lamb2*^{-/-};*Chop*^{-/-} mice versus *Lamb2*^{-/-} mice (Fig. 3*I*). In addition, there was less interstitial fibrosis in *Lamb2*^{-/-};*Chop*^{-/-} mice compared with *Lamb2*^{-/-} mice, as shown by Gomori's Trichrome staining (Fig. 3*I*). Ultrastructural analysis revealed diffuse foot process (FP) effacement (Fig. 3 *J*, *b*, red arrow) and mild

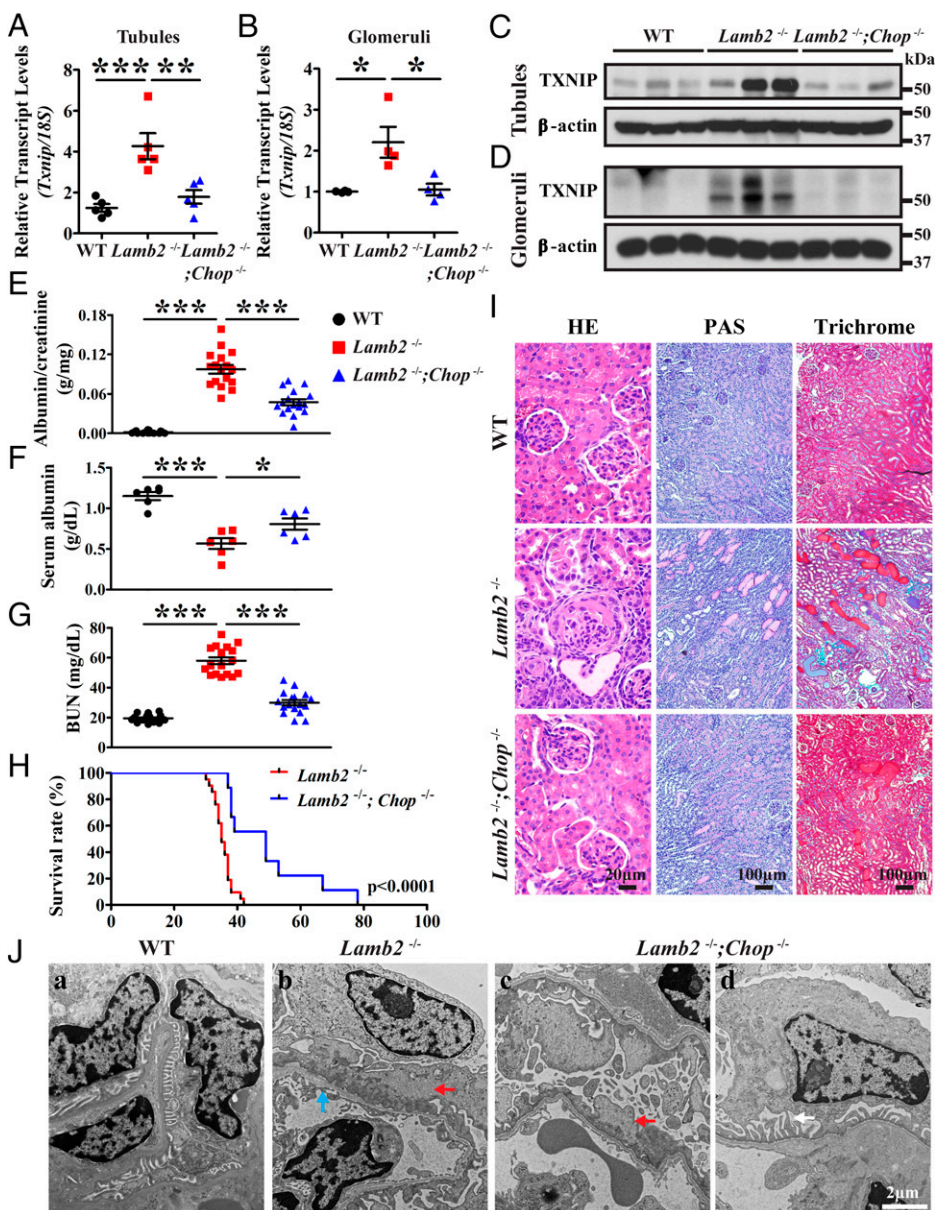


Fig. 3. CHOP deficiency attenuates TXNIP expression and mitigates albuminuria, as well as improves kidney function and life span in *Lamb2*^{-/-} mice. (*A* and *B*) Quantitative PCR analysis of *Txnip* from isolated tubules (*A*) and glomeruli (*B*) of WT, *Lamb2*^{-/-}, and *Lamb2*^{-/-};*Chop*^{-/-} mice at P25. Mean \pm SD ($n = 4$ to 5 mice per genotype). * $P < 0.05$; ** $P < 0.01$; *** $P < 0.001$. (*C* and *D*) Immunoblot to detect TXNIP protein from isolated tubules (*C*) and glomeruli (*D*) of WT, *Lamb2*^{-/-}, and *Lamb2*^{-/-};*Chop*^{-/-} mice at P25. $n = 5$ mice per genotype. (*E*) Urinary albumin/creatinine ratios in WT, *Lamb2*^{-/-}, and *Lamb2*^{-/-};*Chop*^{-/-} mice at P25. Mean \pm SD ($n = 17$ mice per genotype). *** $P < 0.001$. (*F*) Serum albumin levels for the indicated genotypes at P25. Mean \pm SD ($n = 6$ mice per genotype). * $P < 0.05$; *** $P < 0.001$. (*G*) BUN levels from mice of the indicated genotypes at P25. Mean \pm SD ($n = 17$ mice per genotype). *** $P < 0.001$. (*H*) Survival curves of *Lamb2*^{-/-} (red line, $n = 22$) and *Lamb2*^{-/-};*Chop*^{-/-} mice (blue line, $n = 9$). Log-rank test analysis showed a significant difference between the two groups ($P < 0.0005$). (*I*) HE, PAS, and Gomori's Trichrome staining of paraffin kidney sections from WT, *Lamb2*^{-/-}, and *Lamb2*^{-/-};*Chop*^{-/-} mice at P25. (Scale bars, 20 [Left] and 100 μ m [Middle and Right].) (*J*) TEM analysis of the glomerular filtration barrier from mice of the indicated genotypes at P25. Red arrows indicate diffuse FP effacement, white arrow indicates well-preserved podocyte structures without much FP effacement, and blue arrow indicates mild GBM thickening. (Scale bar, 2 μ m.)

GBM thickening (Fig. 3 J, b, blue arrow) in *Lamb2*^{-/-} mice. By contrast, although FP effacement was observed in some glomeruli of *Lamb2*^{-/-};*Chop*^{-/-} mice (Fig. 3 J, c, red arrow), there were still well-preserved glomeruli without much FP effacement (Fig. 3 J, d, white arrow), which is consistent with the lower albuminuria in *Lamb2*^{-/-};*Chop*^{-/-} mice compared with *Lamb2*^{-/-} mice. During the disease progression at P35, the double knockout mice developed heavier albuminuria with higher BUN compared to P25, although the severity of albuminuria and BUN level were still significantly lower than those in the single knockout mice at P35 (SI Appendix, Fig. S5 A and B). In addition, these double knockout mice at the later stage exhibited glomerulosclerosis, abundant protein casts in the renal tubules, and more interstitial fibrosis, as manifested by H&E, PAS, and Trichrome staining, respectively (SI Appendix, Fig. S5 C). In summary, consistent with the proteinuria and kidney function profiles, these studies demonstrate that suppression of CHOP-TXNIP axis in both glomeruli and tubules leads to improvement in glomerular filtration barrier ultrastructure and kidney histopathological features.

CHOP Ablation Blocks TXNIP Shuttling into Mitochondria in Response to Albuminuria. The increasing evidence has indicated that mitochondria act as docking sites for inflammasome assembly. Upon activation, NLRP3 redistributes from the ER to both mitochondria and the mitochondria-associated ER membrane (29). Furthermore, TXNIP is an NLRP3-binding protein, and association of TXNIP with NLRP3 in mitochondria activates inflammasome (29, 30). In human THP1

macrophage and rat INS-1 pancreatic β cell lines, it has been shown that when cells are treated with H₂O₂, oxidative stress can induce subcellular shuttling of TXNIP to mitochondria (29, 31). We therefore set out to study whether under albuminuria-induced ER stress, CHOP would regulate intracellular localization of TXNIP. We purified primary tubular cells from WT, *Lamb2*^{-/-}, and *Lamb2*^{-/-};*Chop*^{-/-} mice at P25. Passages 1 to 2 TECs were treated with 40 mg/mL BSA for 4 h and stained for TXNIP and mitochondria marker MitoTracker, as well as nucleus marker Hoechst 33342, and TXNIP localization was examined by confocal microscopy. In resting cells, TXNIP protein was found to localize to nucleus primarily (Fig. 4A). The localization of TXNIP changed dramatically after treatment with BSA. In WT and *Lamb2*^{-/-} TECs, TXNIP relocated into the perinuclear space and colocalized with Mitotracker, whereas in *Lamb2*^{-/-};*Chop*^{-/-} TECs, TXNIP retained inside the nucleus, and very little colocalization with Mitotracker was detected (Fig. 4A). To confirm that the TXNIP intracellular localization after BSA treatment is impacted by CHOP, subcellular fractionation studies were performed at 8 h after BSA treatment. With this approach, the amount of TXNIP and NLRP3 found in the mitochondrial fractions of *Lamb2*^{-/-};*Chop*^{-/-} TECs was decreased considerably compared to that in *Lamb2*^{-/-} TECs after the treatment of BSA (Fig. 4B). To corroborate the findings in albumin-treated TECs, we isolated mitochondrial fractions from renal tubules of WT, *Lamb2*^{-/-}, and *Lamb2*^{-/-};*Chop*^{-/-} mice at P25. Mitochondrial fractions revealed that deletion of CHOP significantly blocked the increased expression of TXNIP and NLRP3 in

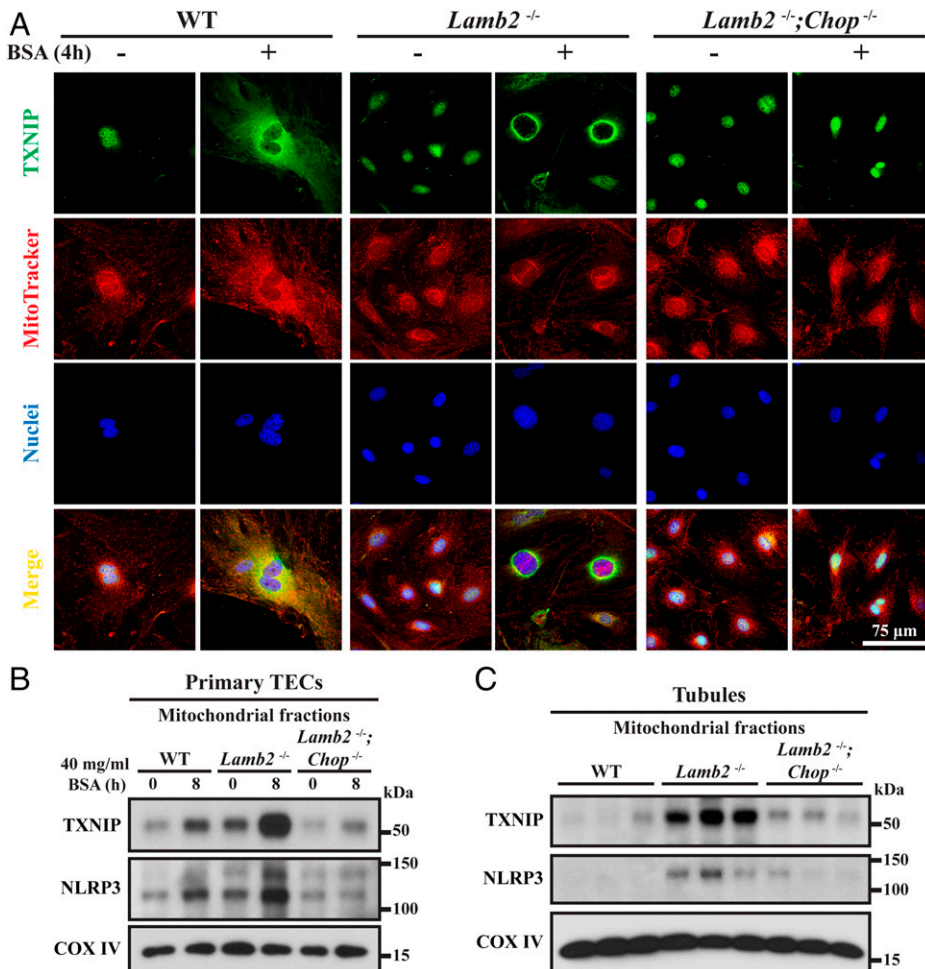


Fig. 4. CHOP deletion blocks albuminuria-induced TXNIP shuttling into mitochondria. (A) Double IF staining of TXNIP (green) and MitoTracker (red) in primary TECs treated without or with 40 mg/mL BSA for 4 h. Nuclei were counterstained with Hoechst 33342 (blue). Individual confocal images were merged digitally. The images shown are representative of four independent experiments. (Scale bar, 75 μ m.) (B) WB analysis of TXNIP and NLRP3 expression in the mitochondrial fractions of primary TECs treated without or with 40 mg/mL BSA for 8 h. COX IV was used as mitochondrial internal control. The WB image shown is representative of at least three independent experiments. (C) Representative immunoblots of TXNIP and NLRP3 expression in the mitochondrial fractions of isolated tubules from WT, *Lamb2*^{-/-}, and *Lamb2*^{-/-};*Chop*^{-/-} mice at P25. COX IV was used as mitochondrial internal control. *n* = 5 mice per genotype.

the mitochondria of *Lamb2*^{-/-} tubules (Fig. 4C). These data indicate that CHOP regulates intracellular translocation of TXNIP to mitochondria in response to albuminuria-induced ER stress.

TXNIP Mediates CHOP-Induced Mitochondrial Reactive Oxygen Species Overproduction and NLRP3 Inflammasome Activation in Albuminuria. TXNIP has been reported to be released from Trx after oxidation of Trx by reactive oxygen species (ROS), which allows TXNIP to bind to the NLRP3 inflammasome (30). This prior study prompted us to determine the role of the CHOP-TXNIP signaling axis in the regulation of production of mitochondrial ROS, the major intracellular sources of ROS (90%), in albuminuria. Primary TECs isolated from WT, *Lamb2*^{-/-}, and *Lamb2*^{-/-};*Chop*^{-/-} mice at P25 were cultured and treated with 40 mg/mL BSA for 90 min and then incubated with Galuminox, a recently identified mitochondrial ROS probe by us, which detects both superoxide and its downstream product, hydrogen peroxide, largely in mitochondria (32). The fluorescence intensity measured by flow cytometry clearly showed that albumin overload stimulated mitochondrial ROS generation in WT, *Lamb2*^{-/-}, and *Lamb2*^{-/-};*Chop*^{-/-}

TECs relative to their respective untreated cells (Fig. 5A and B). In contrast, substantially less mitochondrial ROS production was detected in *Lamb2*^{-/-};*Chop*^{-/-} TECs treated with BSA compared with WT and *Lamb2*^{-/-} TECs treated with BSA (Fig. 5A and B). To directly interrogate the role of TXNIP in mitochondrial ROS generation after albumin overload, PTCs were isolated from adult WT and *Txnip*^{-/-} mice that showed no abnormalities in growth, viability, and reproduction (33). As shown in Fig. 5C and D, although WT PTCs showed a marked induction of TXNIP at both translational and transcriptional levels after treatment with BSA, as expected, *Txnip*^{-/-} PTCs demonstrated a complete depletion of TXNIP in the absence and presence of BSA (Fig. 5C and D). We further confirmed TXNIP deletion in the mitochondrial fraction of *Txnip*^{-/-} PTCs with or without BSA treatment (Fig. 5E). When both WT and *Txnip*^{-/-} PTCs were treated with 40 mg/mL BSA for 90 min, flow cytometry analysis of Galuminox revealed that in contrast to WT PTCs that exhibited a marked increase in mitochondrial ROS levels after treatment with BSA, *Txnip*^{-/-} PTCs did not manifest much increase in mitochondrial ROS levels after exposure to BSA (Fig. 5F).

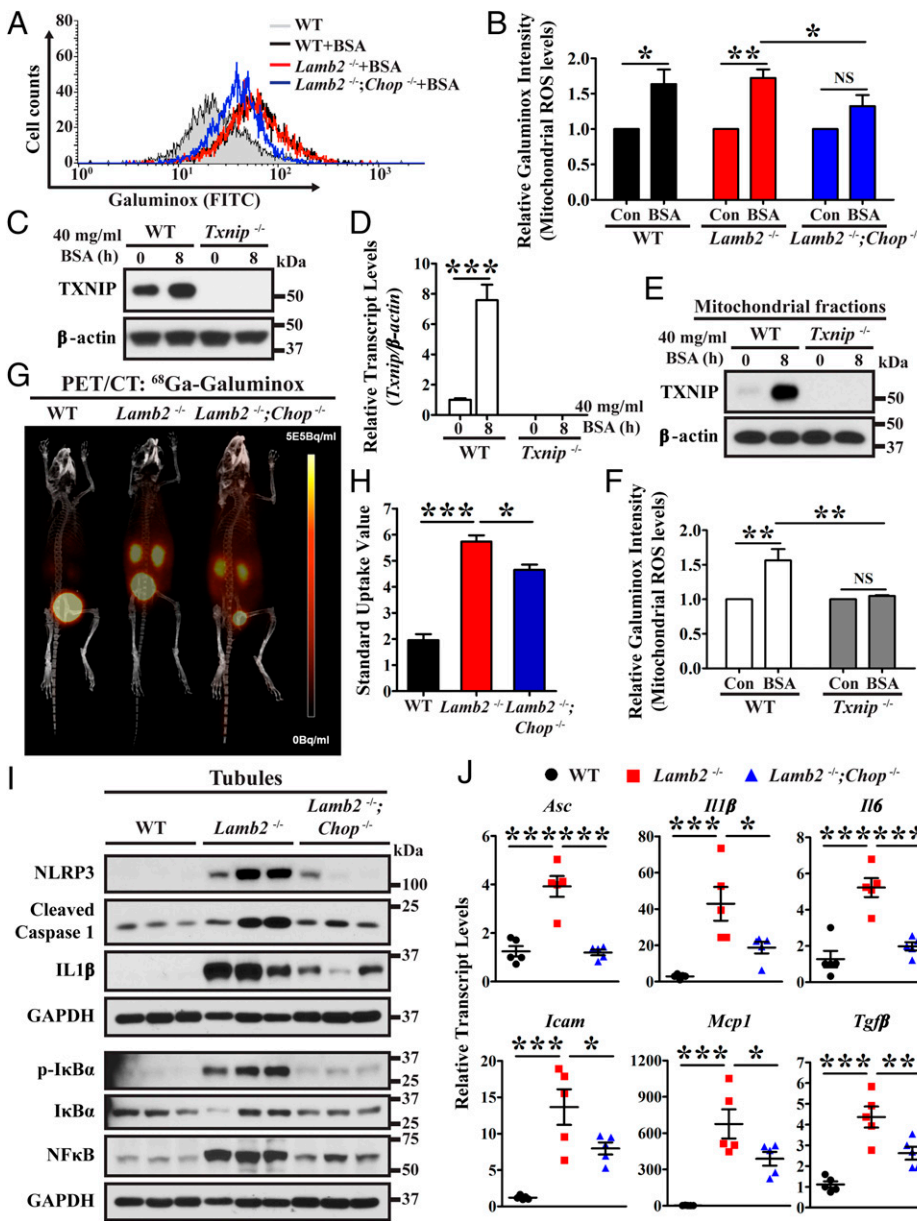


Fig. 5. TXNIP-mediated mitochondrial ROS production and NLRP3 inflammasome activation after albumin overload are suppressed by CHOP depletion. (A and B) Primary TECs from the indicated genotypes were treated with 40 mg/mL BSA for 90 min and then stained with the mitochondrial ROS indicator Galuminox, and the fluorescence intensity was measured by flow cytometry. The relative fluorescence intensity was expressed as mean \pm SD from three independent experiments. NS, not significant; * P < 0.05; ** P < 0.01. Con, control. (C–E) Primary PTCs were isolated and cultured from WT and *Txnip*^{-/-} mice. Cultured PTCs were starved for 16 h and then treated with 40 mg/mL BSA for 8 h. (C) Cell lysates were analyzed by WB for protein levels of TXNIP and β -actin. The WB image shown is representative of at least three independent experiments. (D) Quantitative PCR analysis for mRNA levels of TXNIP. Gene expression was normalized to β -actin. Mean \pm SD from three independent experiments. *** P < 0.001. (E) Mitochondrial fractions were analyzed by WB for protein levels of TXNIP. COX IV was used as mitochondrial internal control. (F) Primary PTCs treated with or without 40 mg/mL BSA for 90 min were stained by Galuminox for mitochondrial ROS levels and assessed by flow cytometry. The relative fluorescence intensity was expressed as mean \pm SD from three independent experiments. ** P < 0.01. (G) ⁶⁸Ga-Galuminox (100 μ Ci) was injected via tail vein into WT, *Lamb2*^{-/-}, and *Lamb2*^{-/-};*Chop*^{-/-} mice at P28. Static PET scans were acquired from 30 to 60 min post-tail vein injection. PET/CT images as shown are a summation of frames from 30 to 45 min. (H) SUV analysis of ⁶⁸Ga-Galuminox uptake in kidneys of the indicated genotypes. Mean \pm SD (n = 4 to 6 kidneys per genotype). * P < 0.05; *** P < 0.001. (I) Representative WBs evaluating expression of NLRP3, cleaved caspase 1, IL-1 β , p-I κ B α , I κ B α , and NF κ B in isolated tubules from the indicated genotypes at P25. n = 3 mice per genotype. (J) Quantitative PCR analysis of isolated tubules for transcript levels of inflammasome and proinflammatory genes. Gene expression was normalized to 18S. Mean \pm SD (n = 5 mice per genotype). * P < 0.05; ** P < 0.01; *** P < 0.001.

These findings collectively suggest that TXNIP is required for mitochondrial ROS production and that attenuated translocation of TXNIP to mitochondria due to CHOP deficiency mediates less pronounced generation of mitochondrial ROS evoked by albumin overload.

To unambiguously prove the suppressed mitochondrial ROS levels in *Lamb2*^{-/-}; *Chop*^{-/-} mice directly in vivo, we took advantage of noninvasive, sensitive, and quantitative PET/CT molecular imaging to detect mitochondrial ROS by employing our newly developed mitochondrial ROS radiotracer ⁶⁸Ga-Galuminos (32). This ⁶⁸Ga-radiotracer (incorporated with a nonconventional, generator-produced isotope) is capable of detecting mitochondrial ROS in vivo. Preclinical PET/CT images (summation of frames over 30 to 45 min) postadministration of ⁶⁸Ga-Galuminos are shown in Fig. 5G. Of note, ⁶⁸Ga-Galuminos showed a 2.9-fold higher uptake in kidneys of *Lamb2*^{-/-} mice (standard uptake value [SUV], 5.73 ± 0.24, *n* = 6) compared with WT littermates (SUV, 1.96 ± 0.23, *n* = 6) and a statistically significant 19% reduction of the uptake in *Lamb2*^{-/-}; *Chop*^{-/-} mice (SUV, 4.65 ± 0.2, *n* = 4) compared to *Lamb2*^{-/-} mice (Fig. 5H).

Mitochondrial ROS-dependent activation of NLRP3 inflammasome is a molecular platform acted upon signs of cellular “danger” to trigger innate immune defenses through maturation of proinflammatory cytokines such as interleukin (IL)-1β and IL-18, which can activate NFκB to further stimulate NLRP3 synthesis. Key components of a functional NLRP3 inflammasome are NLRP3, the adaptor protein (apoptosis-associated speck-like protein containing CARD [ASC]) and caspase-1 (34). Given decreased protein levels of TXNIP and NLRP3 in the mitochondria, in association with suppressed mitochondrial ROS accumulation in *Lamb2*^{-/-}; *Chop*^{-/-} mice, we thus anticipated inhibition of NLRP3 inflammasome in the double null mice responding to albuminuria in NS. To prove this hypothesis, renal tubules were isolated from the different groups of mice at P25. WB revealed decreased abundance of NLRP3 and cleaved caspase-1 and IL-1β, as well as down-regulation of NFκB and p-IκBα (inhibitor of NFκB [IκBα] that is phosphorylated and inactivated) in the double null mice compared with *Lamb2* null mice (Fig. 5A). Consequently, transcript levels of ASC and IL-1β and their downstream proinflammatory cytokines, including IL-6, intercellular adhesion molecule (ICAM), monocyte chemoattractant protein-1 (MCP-1), and transforming growth factor β (TGFβ), were substantially reduced in the double null compared with the single null mice (Fig. 5J). To confirm the contribution of TXNIP in CHOP-induced activation of inflammasomes, we purified PTCs from WT and *Txnip*^{-/-} mice, and cultured PTCs were incubated with 40 mg/mL BSA for 8 and 24 h. Loss of TXNIP abolished albumin-induced inflammasome activation, as evidenced by a reduction of protein levels of NLRP3 and cleaved caspase-1 in the cell lysates (SI Appendix, Fig. S6A), as well as decreased transcript levels of NLRP3 and ASC (SI Appendix, Fig. S6B). As a result, TXNIP deficiency markedly repressed transcript levels of proinflammatory cytokines such as IL-1β, IL-6, MCP-1, and ICAM (SI Appendix, Fig. S6C). Taken together, these studies incorporating quantitative in vivo molecular imaging support the notion that blockade of TXNIP translocation to mitochondria by CHOP depletion during albuminuria leads to decreased mitochondrial ROS production and subsequent NLRP3 inflammasome activation.

Abrogation of CHOP-TXNIP Signaling Dampens ASK1-Mediated Mitochondrial Apoptosis in Albuminuria. Besides regulating the cellular redox state and inflammation, TXNIP may play a crucial role in the signal transduction for apoptosis. Mitochondrial Trx2

binds to apoptosis signal-regulating kinase 1 (ASK1) and inhibits its activity (35). Upon an increase in mitochondrial ROS, critical cysteine residues in Trx2 become oxidized, and ASK1 is liberated from Trx2 binding. The resultant ASK1 autophosphorylation and activation mediate ROS-induced apoptosis in a mitochondria-dependent pathway (36). We thus anticipated that in albuminuria, increased relocation of TXNIP into mitochondria would compete with ASK1 for Trx2 binding, and concomitantly increased mitochondrial ROS levels would further release ASK1 from Trx2, thus promoting mitochondrial apoptosis. To test this hypothesis, we monitored Trx2 and p-ASK1 levels in the mitochondrial fractions of renal tubules isolated from WT, *Lamb2*^{-/-}, and *Lamb2*^{-/-}; *Chop*^{-/-} mice at P25. As shown in Fig. 6A, correlating with increased mitochondrial TXNIP level in *Lamb2*^{-/-} tubules (Fig. 4C), albuminuria provoked a decrease in Trx2 abundance in the mitochondrial fractions of *Lamb2*^{-/-} tubules since oxidized Trx2 is unstable and more accessible for degradation (36, 37), which led to an increase in mitochondrial p-ASK1 abundance (Fig. 6A). Inhibition of the CHOP-TXNIP axis in *Lamb2*^{-/-}; *Chop*^{-/-} tubules reverted the aforementioned changes (Fig. 6A).

In the mitochondria (intrinsic) apoptotic pathway, cytochrome *c* (Cyto *c*), released from the mitochondria into the cytoplasm, forms the “apoptosome” with Apaf-1 and procaspase 9, which in turn induces activation of procaspase 9 and subsequent apoptosis. We observed a marked decrease of Cyto *c* in the mitochondrial fraction (Fig. 6B) and an increase in cleaved, active caspase 9 (Fig. 6B, red arrows) in albuminuria-exposed *Lamb2*^{-/-} tubules versus WT tubules. Repression of CHOP-TXNIP signaling in *Lamb2*^{-/-}; *Chop*^{-/-} tubules alleviated p-ASK1-mediated mitochondrial apoptosis (Fig. 6A and B). TEM ultrastructural analyses of mitochondrial integrity were performed in sections from WT, *Lamb2*^{-/-}, and *Lamb2*^{-/-}; *Chop*^{-/-} mice at P25 (Fig. 6C). In normal renal tubules, mitochondria were aligned in well-preserved rows. Intracellular albumin overload resulted in disorganized and fragmented mitochondrial arrays (Fig. 6C, black arrow) and aggregates of swollen mitochondria (Fig. 6C, white and blue arrows) with mild lysis (Fig. 6C, white arrow) and disrupted cristae (Fig. 6C, blue arrow) in *Lamb2*^{-/-} tubules. In contrast, these ultrastructural derangements observed in *Lamb2*^{-/-} tubules were substantially reversed by CHOP depletion in *Lamb2*^{-/-}; *Chop*^{-/-} tubules (Fig. 6C).

We next investigated whether CHOP deficiency in primary TECs exposed to albumin overload can simulate the in vivo findings. WT, *Lamb2*^{-/-}, and *Lamb2*^{-/-}; *Chop*^{-/-} TECs were treated with 40 mg/mL BSA for 8 h. Similarly, we found that mitochondrial Trx2 baseline level before the albumin treatment was significantly lower in *Lamb2*^{-/-} TECs compared to that in WT or *Lamb2*^{-/-}; *Chop*^{-/-} TECs (Fig. 6D), which was inversely correlated with the mitochondrial TXNIP levels in the primary TECs of the indicated genotypes (Fig. 4B). Although albumin overload for the very short term (8 h) resulted in a slight increase in Trx2 in all groups, the ratio of mitochondrial Trx2/TXNIP in *Lamb2*^{-/-} TECs was substantially decreased compared to that in WT or *Lamb2*^{-/-}; *Chop*^{-/-} TECs (Fig. 6D). A concomitant dramatic increase in ASK1 phosphorylation and a significant reduction of Cyto *c* in the mitochondrial fraction of *Lamb2*^{-/-} TECs was observed (Fig. 6D). Moreover, Cyto *c* leakage from mitochondria led to activation of procaspase 9 (Fig. 6E, red arrows) and executioner caspase 3 (Fig. 6E). Consistent with the in vivo findings, CHOP deletion blocked p-ASK1-mediated mitochondrial dysfunction and apoptosis (Fig. 6D and E). In summary, our results clearly indicate that abolishment of CHOP-TXNIP

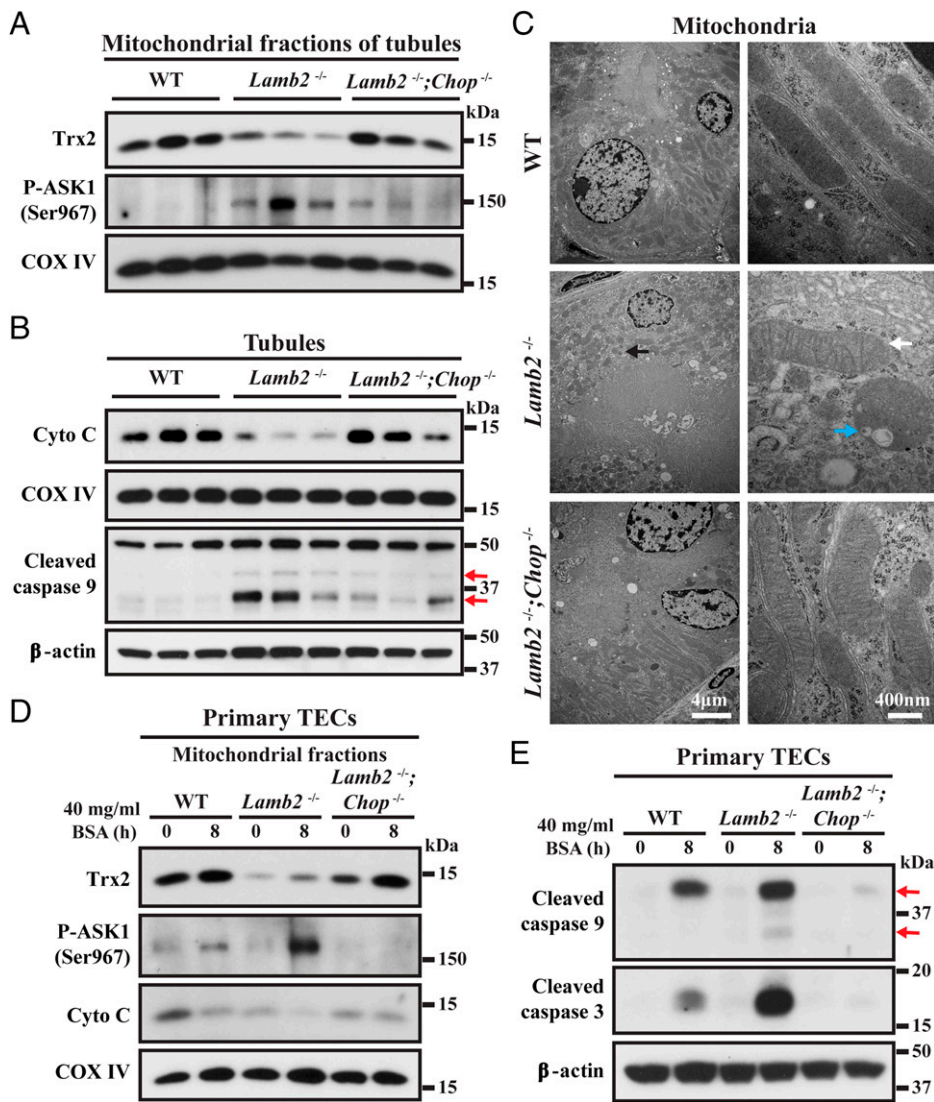


Fig. 6. Inhibition of the CHOP-TXNIP axis alleviates mitochondrial ASK1-mediated intrinsic apoptosis in albuminuria. (A) Representative WBs of Trx2 and p-ASK1 (Ser967) in the mitochondrial fractions of isolated tubules from WT, *Lamb2*^{-/-}, and *Lamb2*^{-/-};*Chop*^{-/-} mice at P25. COX IV was used as mitochondrial internal control. *n* = 5 mice per genotype. (B) Representative WBs of Cyto C from the mitochondrial fractions and cleaved caspase 9 from the whole tubular lysates of the indicated groups at p25. COX IV and β -actin were used as mitochondrial and whole tubular lysate internal control, respectively. Red arrows indicate the cleaved caspase 9. *n* = 5 mice per genotype. (C) TEM ultrastructural analysis of mitochondria in the tubules from mice of the indicated genotypes at P25. Black arrow indicates fragmented mitochondria, white arrow indicates aggregates of swollen mitochondria with mild lysis, and blue arrow indicates disruption of mitochondrial cristae. (Scale bar, 4 μ m [Left] and 400 nm [Right].) (D) Mitochondrial fractions of primary cultured TECs from WT, *Lamb2*^{-/-}, and *Lamb2*^{-/-};*Chop*^{-/-} mice at P25, which were treated without or with 40 mg/mL BSA for 8 h, were analyzed by WBs for levels of Trx2, p-ASK1 (Ser967), and Cyto C. COX IV was used as mitochondrial internal control. (E) Whole-cell lysates of primary cultured TECs from WT, *Lamb2*^{-/-}, and *Lamb2*^{-/-};*Chop*^{-/-} mice at P25, which were treated without or with 40 mg/mL BSA for 8 h, were analyzed by WBs for cleaved caspases 9 and 3. β -actin was used as loading control.

signaling ameliorates p-ASK1-dependent mitochondrial apoptosis in tubular cells in NS.

Discussion

Our present study demonstrates for the first time that CHOP-TXNIP signaling is a key regulator for NLRP3 inflammasome activation and p-ASK1-mediated mitochondrial apoptosis conferred by increased mitochondrial ROS accumulation in NS. Our findings reveal that in response to albuminuria-induced ER stress, CHOP regulates TXNIP subcellular shuttling from nucleus to mitochondria, which is required for mitochondrial ROS production. By utilizing our recently identified molecular imaging probe ⁶⁸Ga-Galuminox through PET/CT imaging, we directly show that CHOP deletion suppresses mitochondrial ROS levels in NS. Our results concur with the notion that mitochondrial TXNIP competes with Trx2 for NLRP3 binding, as well as competes with ASK1 for Trx2 binding. The mitochondrial Trx2 oxidation by mitochondrial ROS releases TXNIP to activate NLRP3 inflammasome, as well as dissociates ASK1 to initiate mitochondria-dependent apoptosis. In addition, it has been shown that oxidant stress and ER stress operate in a positive feedback manner to worsen the tubulointerstitial injury (38, 39). Thus,

CHOP-TXNIP axis modulates ER-mitochondria crosstalk and blockade of TXNIP translocation into mitochondria counteracts deleterious effects of albuminuria in NS (Fig. 7).

Not much is known about the function of mitochondrial Trx2 in kidney disease. Our study suggests that mitochondrial Trx2 plays a unique and critical role in tubular cell survival in NS. Since mitochondria have the most reducing environment among all cellular organelles, a reduced state is critical for maintaining the normal function of many mitochondria proteins (40). Trx2, a small redox protein, contains a redox-active disulfide/dithiol group within the conserved active site sequence Cys-Gly-Pro-Cys and a mitochondria targeting signal peptide. Reduced Trx2 catalyzes the reduction of disulfide bonds in multiple substrate proteins, and oxidized Trx2 is reversibly reduced by the action of Trx reductase and NADPH (41). Homozygous deletion of Trx2 causes massive apoptosis and early embryonic lethality (42). Mice with cardiac-specific Trx2 ablation develop dilated cardiomyopathy at 1 mo, associated with increased mitochondrial ROS generation and increased ASK1 apoptotic signaling (36). Whether overexpression of mitochondrial Trx2 can mitigate NLRP3 inflammasome activation and intrinsic apoptosis in our NS model warrants further investigation.

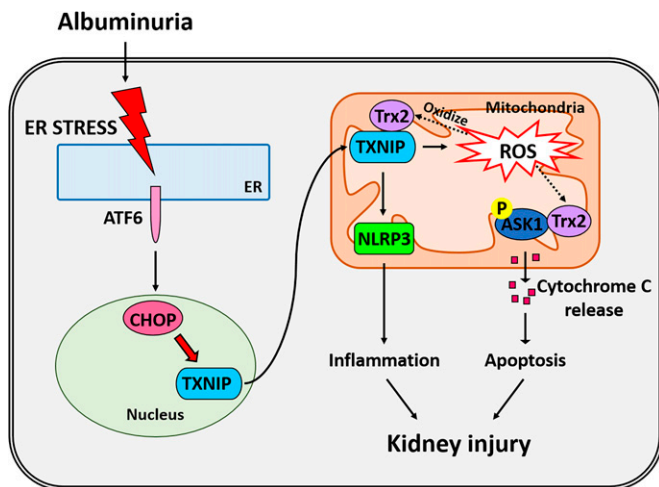


Fig. 7. Scheme depicting that CHOP-TXNIP signaling axis in renal tubular cells modulates mitochondria-dependent NLRP3 inflammasome activation and mitochondrial p-ASK1-mediated intrinsic apoptosis in NS.

In the current study, we also discover that removing ASK1 from Trx2 inhibition due to TXNIP relocation to mitochondria triggers mitochondria-dependent apoptosis in renal tubules in NS. This finding has direct translational potential. ASK1, a serine/threonine kinase, is a member of the 28 MAPKKK family and activated in response to proinflammatory stimuli, ROS, and cellular stress leading to apoptosis (43). ASK1 is localized in the cytosol as well as in mitochondria, where it binds to cytosolic Trx1 and mitochondrial Trx2, respectively. Its activity is regulated by phosphorylation/dephosphorylation whereby phosphorylation of serine 967 results in activation of ASK1. Once proapoptotic stimuli dissociate Trx1 or Trx2 from ASK1, ASK1 in cytoplasm mediates a JNK-dependent while ASK1 in mitochondria mediates a JNK-independent apoptotic pathway (35). In our NS model, we do not observe JNK activation (*SI Appendix, Fig. S2B*), indicating that mitochondrial ASK1 is a key mediator inducing cell death in NS. Selonsertib, a kinase inhibitor targeted to ASK1, has been evaluated in a phase 2 clinical trial for its safety and efficacy in adults with treatment-refractory moderate-to-advanced diabetic kidney disease. Exploratory post hoc analyses suggest that selonsertib may slow eGFR decline over one year, and no dose-dependent adverse effects are observed during the 1-y trial period (44). It would be worthwhile to investigate whether Selonsertib has any effect on NS mouse models and patients. Moreover, a nontoxic small molecule compound, SRI-37330, was recently discovered as a novel TXNIP inhibitor to repress its promoter activity. The exciting results that SRI-37330 treatment leads to a marked improvement in glucose homeostasis in mouse models of obesity- and streptozotocin-induced diabetes would drive us to test whether this chemical compound has therapeutic potential in the treatment of NS.

In conclusion, we provide a report that CHOP-TXNIP is a critical mediator linking ER stress and mitochondria dysfunction during heavy albuminuria and ensuing tubulointerstitial fibrosis. Targeting TXNIP may provide an attractive approach that is distinctive from the currently available ACEIs/ARBs to attenuate the detrimental effect of albuminuria in NS.

Materials and Methods

Mice. *Lamb2*^{-/-} mice have been described previously (45, 46). *Txnip*^{-/-} mice were provided by Roger Davis (San Diego State University, San Diego, CA) (33).

Chop^{-/-} mice on the C57BL/6 genetic background (stock no. 005530) were purchased from the Jackson Laboratory. All animal experiments conformed to the NIH Guide for the Care and Use of Laboratory Animals and were approved by the Washington University Animal Studies Committee. Mice were maintained on a 12-h light/dark cycle at 18 to 26 °C in an American Association for Accreditation of Laboratory Animal Care (AAALAC) accredited facility. Both male and female littermates ranging in age from 3 to 6 wk were used for experiments. For survival experiments, male and female mutant mice were followed up to 12 wk after birth.

Renal Biopsies. Renal biopsy samples were obtained from Washington University Kidney Translational Research Core. The analyzed kidney biopsies were from adult patients with a diagnosis of FSGS or MN, as determined by IF staining, H&E staining, PAS staining, PAS-methenamine silver staining, and electron microscopy. All patients exhibited nephrotic range proteinuria at the time of biopsy. The paracarcinoma normal kidney tissues were used as controls.

Isolation of Mouse Glomeruli and Tubules. WT, *Lamb2*^{-/-}, and *Lamb2*^{-/-}; *Chop*^{-/-} mice at P25 were perfused through the heart with magnetic 4.5- μ m-diameter Dynabeads (Invitrogen). Kidneys were minced into small pieces, digested by collagenase A (Sigma-Aldrich) and DNase I (Sigma-Aldrich). The glomeruli were filtered and collected using a magnet. The purity of glomeruli was >95%. The remaining tubulointerstitial tissue was centrifuged for 15 min at 1,000 \times *g* (47). The resulting pellets were divided and shock-frozen for RNA and protein extraction or for primary TEC cell culture.

Primary Cell Isolation, Culture, and Treatments. Primary podocytes from WT and *Lamb2*^{-/-} mice were prepared as previously described (48). Briefly, isolated glomeruli were plated onto collagen type I-coated culture dishes and cultured in 5% CO₂ at 37 °C in DMEM (Gibco): Ham's F-12 (Lonza) (2:1) containing 3T3-L1 supernatant, 5% FBS (Gibco), 1% Insulin-Transferrin-Selenium (ITS) supplement (Gibco), and 100 U/mL penicillin-streptomycin (Gibco). After 3 d, cell colonies began to sprout around the glomeruli. These cells (P0) showed an epithelial morphology with a polyhedral shape when confluence was reached.

After primary TECs were isolated from WT, *Lamb2*^{-/-}, and *Lamb2*^{-/-}; *Chop*^{-/-} mice as described above, single-cell suspension was obtained by pipetting the isolated tubules and filtering through a 40- μ m strainer. The filtrated cells were resuspended and cultured in 5% CO₂ at 37 °C in DMEM/F-12 (Gibco) medium containing 5% FBS (Gibco), 0.7% ITS supplement (Gibco), 10 ng/mL epidermal growth factor (Sigma-Aldrich), 4 μ g/mL dexamethasone (Sigma-Aldrich), 50 μ M L-ascorbic-2 phosphate (Sigma-Aldrich), and 100 U/mL penicillin-streptomycin (Gibco) (49).

Primary PTCs from WT and *Txnip*^{-/-} mice were isolated using the established method (50). Briefly, kidneys were removed from PBS-perfused mice, minced, and incubated for 30 min in PBS containing collagenase type 1 (Sigma-Aldrich) and DNase I (Sigma-Aldrich). The reaction was terminated by adding DMEM/F-12 (Gibco) medium with 10% FBS, and single-cell suspension was obtained by pipetting the tissue and filtering through a 40- μ m strainer. Lotus tetragonolobus lectin (LTL)-positive PTCs were separated from the single-cell suspension using the Dynabeads magnetic bead conjugation system, whereby biotinylated, anti-LTL (Vector Laboratories) was incubated with Dynabeads Biotin Binder (Thermo Fisher) at 4 °C for 45 min. Beads were then washed twice with 1% BSA/PBS buffer and incubated with the single-cell suspension in a final volume of 1 mL at 4 °C for 45 min. Beads and LTL-positive cells were then trapped against a magnet, and residual LTL-negative cells were washed away. The cells were cultured in the same medium as used for TECs.

Podocytes, TECs, and PTCs at passage 1 or 2 were used for experiments. Before BSA treatment, cells were starved for 16 h and then stimulated with 20 or 40 mg/mL fatty acid-free and low-endotoxin BSA (Sigma-Aldrich) in serum-free medium for different time durations.

Mitochondrial Fractionation. Fresh tubules and cultured cells were washed with cold PBS first. Mitochondrial fractions were isolated from tubules using Mitochondria Isolation Kit for Tissue and from TECs or PTCs using Mitochondrial Isolation Kit for Cultured Cells (Thermo Fisher Scientific) according to the manufacturer's protocols.

Antibodies. Commercially available antibodies were obtained as follows: anti-caspase 12, anti-caspase 3, anti-caspase 9, anti-cleaved caspase 1, anti-p-JNK, anti-JNK, anti-p-eIF2 α , anti-eIF2 α , anti-I κ B α , anti-CHOP, anti-NLRP3, anti-COX IV, anti-IL1 β , anti-cleaved caspase1, anti-p-I κ B, anti-I κ B, anti-NF κ B, and anti-cytochrome

c antibodies were from Cell Signaling Technology; anti-ATF6 and anti-p-IRE1 α antibodies were from Novus Biological; anti-p-ASK1(Ser967) antibody was from Sigma-Aldrich; anti-XBP1s antibody was from BioLegend; anti-TXNIP antibody was from MBL International Corporation; anti-WT-1 antibodies were from Santa Cruz Biotechnology or Abcam; and anti-ATF4 and anti-Trx2 antibodies were from Santa Cruz Biotechnology. HRP-conjugated anti-mouse β -actin antibody was from Sigma-Aldrich and HRP-conjugated secondary antibodies were from Cell Signaling Technology.

Western Blot Analysis. Isolated glomeruli and tubules, primary podocytes, TECs, and PTCs were lysed by RIPA buffer (Cell Signaling Technology) containing protease inhibitor mixture (Sigma-Aldrich) and phosphatase inhibitor tablets (Roche). The protein concentrations of tissue and cell lysates were determined by Bio-Rad Protein assay using BSA as a standard. WBs were performed as previously described (48). Protein band intensities were quantified using Image J software.

Measurement of Mitochondrial ROS Levels. The mitochondrial ROS levels were measured by Galunox (32). TECs and PTCs of different genotypes were stained with 20 μ M Galunox at 37 $^{\circ}$ C in the dark for 1 h. After incubation, the cells were washed with PBS. Fluorescence was measured by a Calibur 3 flow cytometer (BD Biosciences) at the fluorescence-activated cell sorting core facility of the Washington University School of Medicine. The results were analyzed by the CellQuest program.

IF Staining and Confocal Microscopy. Frozen sections were fixed with 4% paraformaldehyde in PBS for 5 min at room temperature and blocked with 1% normal BSA for 1 h at room temperature. IF staining on paraffin sections with citrate (pH 6.0) antigen retrieval was performed as described previously (51). For TXNIP staining, the slides were stained with mouse IgG1 anti-TXNIP antibody (MBL) overnight at 4 $^{\circ}$ C. For albumin staining, the slides were incubated with a goat anti-albumin (R&D Systems) antibody together with a rabbit anti-Lam α 5 (a kind gift from Jeffrey Miner, Washington University School of Medicine, St. Louis, MO) or a rabbit anti-WT1 (Santa Cruz Biotechnology) antibody overnight at 4 $^{\circ}$ C. Slides were analyzed under a fluorescence microscope (Nikon).

For immunocytochemistry, TECs were seeded on coverslips coated with 5 mg/mL rat collagen I (Trevigen) in 24-well plates. The cells were treated with 250 nM MitoTracker Red CMXRos (Invitrogen) at 37 $^{\circ}$ C for 20 min and then fixed with 4% paraformaldehyde for 10 min, permeabilized with 0.1% Triton X-100 for 5 min, and blocked with 1% BSA for 30 min at room temperature, followed by incubation with the mouse IgG1 anti-TXNIP antibody overnight. The slides were washed with PBS and incubated with Alexa 488-conjugated secondary antibody (Molecular Probes) and Hoechst 33342 to stain nuclei. The slides were then mounted with anti-bleed solution and visualized using Nikon A1Rsi Confocal Microscopy. Images were acquired with NIS-Elements AR software (Nikon) and analyzed using Image J software (NIH).

Light and Electron Microscopy. For light microscopy, kidneys were fixed in 4% paraformaldehyde, dehydrated through graded ethanols, embedded in paraffin, sectioned at 4 mm, and stained with H&E, PAS, and Gomori's Trichrome by the Morphology Core. For TEM, tissues were fixed, embedded in plastic, sectioned, and stained as described previously (51).

Preclinical PET/CT Imaging. Radiolabeled 68 Ga-Galunox was synthesized using a procedure described previously (32). Imaging studies were performed in WT, *Lamb2* $^{-/-}$, and *Lamb2* $^{-/-};Chop$ $^{-/-}$ mice at P28. Both sexes were used. For these studies, mice were anesthetized with isoflurane (2%) via an induction chamber and maintained with a nose cone. After anesthetization, the mice were secured in a supine position and placed in an acrylic imaging tray. Following intravenous tail vein administration of 68 Ga-Galunox (100 μ L; 100 μ Ci; 2% ethanol in saline, 3.7 MBq), static preclinical PET scans were performed over 30 to 60 min, using Inveon PET/CT scanner (Siemens Medical Solutions). PET data were stored in list mode, and reconstruction was performed using a Three Dimensional-Ordered Subset Expectation Maximization (3D-OSEM) method with detector efficiency, decay, dead time, attenuation, and scatter corrections applied. For anatomical visualization, PET images were also coregistered with CT images from an Inveon PET/CT scanner. Regions of interests were drawn over the kidney, and SUVs were calculated as the mean radioactivity per injected dose per animal weight.

Urine and Serum Analysis. Urine samples were collected by manual restraint or using a metabolic cage. Blood samples were collected from the tail vein.

Urinary creatinine concentration was quantified by a QuantiChrom creatinine assay kit (BioAssay Systems). Urinary albumin and serum albumin concentrations were measured by a QuantiChrom albumin assay kit (BioAssay Systems). BUN levels were measured by using a QuantiChrom urea assay kit (BioAssay Systems).

mRNA Quantification by Real-Time PCR. Total RNA from isolated glomeruli, tubules, PTCs, or TECs was extracted using the RNeasy kit (QIAGEN) and then reverse-transcribed using an RT-PCR Kit (Superscript III; Invitrogen). Gene expression was evaluated by quantitative real-time PCR with SYBR Green PCR Master Mix (Qiagen) in an Applied Biosystems QuantStudio 6 Flex Real-Time PCR System (Thermo Fisher Scientific) using mouse 18s rRNA or β -actin as an internal control. Quantitative PCR was conducted in triplicates for each sample. Primer sequences are provided in *SI Appendix, Table 1*.

CHOP Putative Binding Site Analysis. ATAC-seq peaks and bigwig files from Cusanovich et al. (25) were downloaded from the Cistrome DB (cistrome.org/) (52, 53). CHOP PWM MA0019.1 was obtained from the JASPAR database (<https://jaspar.genereg.net>). PWM MA0019.1 was used as input for Patser program (28) to identify candidate CHOP bindings sites in the TXNIP genomic sequence using parameter -c -d2 -li. The Patser program calculates the probability of observing a sequence with a particular score or greater for the given matrix and determines the default cutoff score based on sample size-adjusted information content of each PWM. Motif positions were converted to BED file format. ATAC-seq signal files and motif position files were loaded to The Integrative Genomics Viewer (54) for visualization and figuration generation.

NephroSeq Dataset. Data were obtained from the NephroSeq database, version 5. TXNIP gene expression data were downloaded for "Disease vs. Control Analyses," "GFR Analyses," and "Proteinuria Analyses." The data of "Disease vs. Control" and "Proteinuria" were filtered for $P < 0.05$ and fold change > 1.5 , and the graph was visualized using ggplot2. The correlation data of "GFR" and "Proteinuria" were filtered for $P < 0.05$, $\gamma < -0.5$, and $P < 0.05$, $\gamma > 0.5$, respectively.

Statistics. Statistical analyses were performed using GraphPad Prism 5 software. Data were expressed as mean \pm SD of three or more independent experiments. A two-tailed Student's t test was used to compare two groups. One-way ANOVA with post hoc Tukey test was used to compare multiple groups. $P < 0.05$ was considered statistically significant.

Data Availability. All study data are included in the article and *SI Appendix*.

ACKNOWLEDGMENTS. We thank Musculoskeletal Research Center Morphology Core (supported by NIH grant P30AR057235) for histology. We thank Dr. Meei-Hua Lin for advice on cellular staining and confocal microscopy use. Mice were housed in the Washington University Mouse Genetics Core. T.M.G. and G.Z. are supported by NIH grants R03AG070474 and R01NS123571. F.U. is supported by NIH grants R01 DK112921 and UH2 TR002065. V.S. is supported by grants R01 HL111163, R01 HL142297, and NIBIB P41 EB025815. Y.M.C. is supported by NIH grants R01 DK105056A1, R03DK106451, and K08DK089015; the Office of the Assistant Secretary of Defense for Health Affairs through the Peer Reviewed Medical Research Program under award W81XWH-19-1-0320; George M. O'Brien Kidney Research Core Centers (Northwestern University (NU) GoKidney, NIH grant P30 DK114857; University of Alabama at Birmingham (UAB)/University of California San Diego (UCSD), NIH grant P30 DK079337); Mallinckrodt Challenge Grant; Faculty Scholar Award (MD-FR-2013-336) from the Children's Discovery Institute of Washington University and St. Louis Children's Hospital; and Career Development Award from the Nephrotic Syndrome Study Network (NEPTUNE). Y.M.C. is a member of Washington University Institute of Clinical and Translational Sciences (grant UL1 TR000448) and Diabetes Research Center (NIH grant P30 DK020579). The authors thank the Preclinical Imaging Facility at Mallinckrodt Institute of Radiology for help in performing PE/CT imaging studies. The Preclinical Imaging Facility is supported by the Siteman Cancer Center Support Grant (P30CA091842).

Author affiliations: ^aDivision of Nephrology, Department of Medicine, Washington University School of Medicine, St. Louis, MO 63110; ^bDepartment of Biomedical Engineering, Case Western Reserve University, Cleveland, OH 44106; ^cMallinckrodt Institute of Radiology, Washington University School of Medicine, St. Louis, MO 63110; ^dDepartment of Neuroscience, Washington University School of Medicine, St. Louis, MO

63110; ^aDepartment of Pathology and Immunology, Washington University School of Medicine, St. Louis, MO 63110; ^bDivision of Endocrinology, Metabolism, and Lipid Research, Department of Medicine, Washington University School of Medicine, St. Louis, MO 63110; ^cDepartment of Neurology, Washington University School of Medicine, St. Louis, MO 63110; ^dDepartment of Biomedical Engineering, School of Engineering & Applied Science, Washington University, St. Louis, MO 63105; and ^eDepartment of Cell Biology & Physiology, Washington University School of Medicine, St. Louis, MO 63110

1. J. Radhakrishnan *et al.*; CDC-CKD Surveillance Team; European CKD Burden Consortium; CKD.QLD group, Taming the chronic kidney disease epidemic: A global view of surveillance efforts. *Kidney Int.* **86**, 246–250 (2014).
2. S. Sharma, B. Smyth, From proteinuria to fibrosis: An update on pathophysiology and treatment options. *Kidney Blood Press. Res.* **46**, 411–420 (2021).
3. E. I. Christensen, H. Birn, Megalin and cubilin: Synergistic endocytic receptors in renal proximal tubule. *Am. J. Physiol. Renal Physiol.* **280**, F562–F573 (2001).
4. V. Tenten *et al.*, Albumin is recycled from the primary urine by tubular transcytosis. *J. Am. Soc. Nephrol.* **24**, 1966–1980 (2013).
5. E. Erkan, P. Devarajan, G. J. Schwartz, Apoptotic response to albumin overload: Proximal vs. distal/collecting tubule cells. *Am. J. Nephrol.* **25**, 121–131 (2005).
6. K. El Karoui *et al.*, Endoplasmic reticulum stress drives proteinuria-induced kidney lesions via Lipocalin 2. *Nat. Commun.* **7**, 10330 (2016).
7. M. T. Lindenmeyer *et al.*, Proteinuria and hyperglycemia induce endoplasmic reticulum stress. *J. Am. Soc. Nephrol.* **19**, 2225–2236 (2008).
8. T. Ohse *et al.*, Albumin induces endoplasmic reticulum stress and apoptosis in renal proximal tubular cells. *Kidney Int.* **70**, 1447–1455 (2006).
9. X. Wu, Y. He, Y. Jing, K. Li, J. Zhang, Albumin overload induces apoptosis in renal tubular epithelial cells through a CHOP-dependent pathway. *OMICS* **14**, 61–73 (2010).
10. D. Ron, P. Walter, Signal integration in the endoplasmic reticulum unfolded protein response. *Nat. Rev. Mol. Cell Biol.* **8**, 519–529 (2007).
11. W. H. Landschulz, P. F. Johnson, S. L. McKnight, The DNA binding domain of the rat liver nuclear protein C/EBP is bipartite. *Science* **243**, 1681–1688 (1989).
12. M. Ubeda *et al.*, Stress-induced binding of the transcriptional factor CHOP to a novel DNA control element. *Mol. Cell. Biol.* **16**, 1479–1489 (1996).
13. P. Patwari, L. J. Higgins, W. A. Chutkan, J. Yoshioka, R. T. Lee, The interaction of thioredoxin with Txnip. Evidence for formation of a mixed disulfide by disulfide exchange. *J. Biol. Chem.* **281**, 21884–21891 (2006).
14. C. M. Osowski *et al.*, Thioredoxin-interacting protein mediates ER stress-induced β cell death through initiation of the inflammasome. *Cell Metab.* **16**, 265–273 (2012).
15. G. Xu, J. Chen, G. Jing, A. Shalev, Thioredoxin-interacting protein regulates insulin transcription through microRNA-204. *Nat. Med.* **19**, 1141–1146 (2013).
16. J. M. Abais *et al.*, Nod-like receptor protein 3 (NLRP3) inflammasome activation and podocyte injury via thioredoxin-interacting protein (TXNIP) during hyperhomocysteinemia. *J. Biol. Chem.* **289**, 27159–27168 (2014).
17. A. Shah *et al.*, Thioredoxin-interacting protein deficiency protects against diabetic nephropathy. *J. Am. Soc. Nephrol.* **26**, 2963–2977 (2015).
18. M. Zenker *et al.*, Congenital nephrosis, mesangial sclerosis, and distinct eye abnormalities with microcoria: An autosomal recessive syndrome. *Am. J. Med. Genet. A* **130A**, 138–145 (2004).
19. B. G. Hinkes *et al.*; Arbeitsgemeinschaft für Paediatrische Nephrologie Study Group, Nephrotic syndrome in the first year of life: Two thirds of cases are caused by mutations in 4 genes (NPHS1, NPHS2, WT1, and LAMB2). *Pediatrics* **119**, e907–e919 (2007).
20. J. H. Miner, Renal basement membrane components. *Kidney Int.* **56**, 2016–2024 (1999).
21. J. H. Miner, G. Go, J. Cunningham, B. L. Patton, G. Jarad, Transgenic isolation of skeletal muscle and kidney defects in laminin beta2 mutant mice: Implications for Pierson syndrome. *Development* **133**, 967–975 (2006).
22. M. C. Wagner *et al.*, Proximal tubules have the capacity to regulate uptake of albumin. *J. Am. Soc. Nephrol.* **27**, 482–494 (2016).
23. I. M. Schiebl *et al.*, Intravital imaging reveals angiotensin II-induced transcytosis of albumin by podocytes. *J. Am. Soc. Nephrol.* **27**, 731–744 (2016).
24. A. Upadhyay *et al.*, Inflammation, kidney function and albuminuria in the Framingham Offspring cohort. *Nephrol. Dial. Transplant.* **26**, 920–926 (2011).
25. D. A. Cusanovich *et al.*, A single-cell atlas of in vivo mammalian chromatin accessibility. *Cell* **174**, 1309–1324.e18 (2018).
26. O. Fornes *et al.*, JASPAR 2020: Update of the open-access database of transcription factor binding profiles. *Nucleic Acids Res.* **48** (D1), D87–D92 (2020).
27. M. T. Weirauch *et al.*, Determination and inference of eukaryotic transcription factor sequence specificity. *Cell* **158**, 1431–1443 (2014).

Author contributions: S.-J.P. and Y.M.C. designed research; S.-J.P., Y.K., C.L., and J. Suh performed research; J. Sivapackiam, T.M.G., G.J., G.Z., F.U., and V.S. contributed new reagents/analytic tools; S.-J.P., J. Sivapackiam, T.M.G., and Y.M.C. analyzed data; and S.-J.P., G.Z., and Y.M.C. wrote the paper.

Competing interest statement: J. Sivapackiam and V.S. are inventors on a nonprovisional patent, “PET Tracers for Noninvasive Imaging of ROS Activity,” filed by Washington University in St. Louis, St. Louis, MO. All other authors declare no competing or financial interests.

28. G. Z. Hertz, G. D. Stormo, Identifying DNA and protein patterns with statistically significant alignments of multiple sequences. *Bioinformatics* **15**, 563–577 (1999).
29. R. Zhou, A. S. Yazdi, P. Menu, J. Tschopp, A role for mitochondria in NLRP3 inflammasome activation. *Nature* **469**, 221–225 (2011).
30. R. Zhou, A. Tardivel, B. Thorens, I. Choi, J. Tschopp, Thioredoxin-interacting protein links oxidative stress to inflammasome activation. *Nat. Immunol.* **11**, 136–140 (2010).
31. G. Saxena, J. Chen, A. Shalev, Intracellular shuttling and mitochondrial function of thioredoxin-interacting protein. *J. Biol. Chem.* **285**, 3997–4005 (2010).
32. J. Sivapackiam *et al.*, Galuninox: Preclinical validation of a novel PET tracer for non-invasive imaging of oxidative stress in vivo. *Redox Biol.* **37**, 101690 (2020).
33. S. T. Hui *et al.*, Txnip balances metabolic and growth signaling via PTEN disulfide reduction. *Proc. Natl. Acad. Sci. U.S.A.* **105**, 3921–3926 (2008).
34. K. Schroder, J. Tschopp, The inflammasomes. *Cell* **140**, 821–832 (2010).
35. R. Zhang *et al.*, Thioredoxin-2 inhibits mitochondria-located ASK1-mediated apoptosis in a JNK-independent manner. *Circ. Res.* **94**, 1483–1491 (2004).
36. Q. Huang *et al.*, Thioredoxin-2 inhibits mitochondrial reactive oxygen species generation and apoptosis stress kinase-1 activity to maintain cardiac function. *Circulation* **131**, 1082–1097 (2015).
37. X. Chen, H. J. Zhou, Q. Huang, L. Lu, W. Min, Novel action and mechanism of auranofin in inhibition of vascular endothelial growth factor receptor-3-dependent lymphangiogenesis. *Anticancer. Agents Med. Chem.* **14**, 946–954 (2014).
38. I. Sharma, F. Deng, Y. Liao, Y. S. Kanwar, Myo-inositol Oxygenase (MIOX) overexpression drives the progression of renal tubulointerstitial injury in diabetes. *Diabetes* **69**, 1248–1263 (2020).
39. T. Tominaga *et al.*, Myo-inositol oxygenase accentuates renal tubular injury initiated by endoplasmic reticulum stress. *Am. J. Physiol. Renal Physiol.* **316**, F301–F315 (2019).
40. J. M. Hansen, Y. M. Go, D. P. Jones, Nuclear and mitochondrial compartmentation of oxidative stress and redox signaling. *Annu. Rev. Pharmacol. Toxicol.* **46**, 215–234 (2006).
41. A. Holmgren, Antioxidant function of thioredoxin and glutaredoxin systems. *Antioxid. Redox Signal.* **2**, 811–820 (2000).
42. L. Nonn, R. R. Williams, R. P. Erickson, G. Powis, The absence of mitochondrial thioredoxin 2 causes massive apoptosis, exencephaly, and early embryonic lethality in homozygous mice. *Mol. Cell. Biol.* **23**, 916–922 (2003).
43. H. Ichijo *et al.*, Induction of apoptosis by ASK1, a mammalian MAPKKK that activates SAPK/JNK and p38 signaling pathways. *Science* **275**, 90–94 (1997).
44. G. M. Chertow *et al.*; GS-US-223-1015 Investigators, Effects of selonsertib in patients with diabetic kidney disease. *J. Am. Soc. Nephrol.* **30**, 1980–1990 (2019).
45. G. Jarad, J. Cunningham, A. S. Shaw, J. H. Miner, Proteinuria precedes podocyte abnormalities in *Lamb2*^{-/-} mice, implicating the glomerular basement membrane as an albumin barrier. *J. Clin. Invest.* **116**, 2272–2279 (2006).
46. P. G. Noakes *et al.*, The renal glomerulus of mice lacking α -laminin/laminin beta 2: Nephrosis despite molecular compensation by laminin beta 1. *Nat. Genet.* **10**, 400–406 (1995).
47. S. Hakrrouch *et al.*, Effects of increased renal tubular vascular endothelial growth factor (VEGF) on fibrosis, cyst formation, and glomerular disease. *Am. J. Pathol.* **175**, 1883–1895 (2009).
48. S. J. Park *et al.*, Discovery of endoplasmic reticulum calcium stabilizers to rescue ER-stressed podocytes in nephrotic syndrome. *Proc. Natl. Acad. Sci. U.S.A.* **116**, 14154–14163 (2019).
49. E. Kefaloyianni *et al.*, ADAM17 substrate release in proximal tubule drives kidney fibrosis. *JCI Insight* **1**, 87023 (2016).
50. B. G. Johnson *et al.*, Uromodulin p.Cys147Trp mutation drives kidney disease by activating ER stress and apoptosis. *J. Clin. Invest.* **127**, 3954–3969 (2017).
51. Y. M. Chen *et al.*, Laminin β 2 gene missense mutation produces endoplasmic reticulum stress in podocytes. *J. Am. Soc. Nephrol.* **24**, 1223–1233 (2013).
52. S. Mei *et al.*, Cistrome Data Browser: A data portal for ChIP-Seq and chromatin accessibility data in human and mouse. *Nucleic Acids Res.* **45** (D1), D658–D662 (2017).
53. R. Zheng *et al.*, Cistrome Data Browser: Expanded datasets and new tools for gene regulatory analysis. *Nucleic Acids Res.* **47** (D1), D729–D735 (2019).
54. J. T. Robinson *et al.*, Integrative genomics viewer. *Nat. Biotechnol.* **29**, 24–26 (2011).